npj | quantum information

Article

Published in partnership with The University of New South Wales

https://doi.org/10.1038/s41534-026-01333-9

Asynchronous multi-photon interference for quantum networks

Check for updates

Baghdasar Baghdasaryan[1] ✉, Karen Lozano-Méndez[2], Markus Leipe[1,2], Meritxell Cabrejo-Ponce[1,2], Sabine Häussler[1,2], Kaushik Joarder[1], Tim Gühring[2], Stephan Fritzsche[3,4], Thorsten A. Goebel[1,2], Ria G. Krämer[1], Stefan Nolte[1,2], Carlos Andres Melo Luna[2], Yoshiaki Tsujimoto[5] & Fabian Steinlechner[1,2] ✉

Abstract: Advanced quantum communication protocols require high-visibility quantum interference between photons generated at distant nodes, which places stringent demands on optical synchronization. Conventionally, synchronization of optical wave packets relies on pulsed sources and precise optical path stabilization. An alternative approach employs continuous-wave (CW) photon-pair sources, where temporal indistinguishability of photons is enforced by post-selecting detection events within a coincidence window τ_w shorter than the photon coherence time T_c. Despite its conceptual simplicity, the quantitative relation between relevant time scales, achievable interference visibility, and usable multi-photon rates has remained unclear. Here, we develop in detail and experimentally validate a theoretical framework that quantitatively describes time-resolved multi-photon interference in the CW regime. We explicitly incorporate detector timing jitter, photon coherence time, and temporal post-selection. The model is verified using four-photon Hong-Ou-Mandel interference measurements. Based on this validated framework, we determine the coincidence window that maximizes usable four-photon rates for a target interference visibility. Finally, we compare CW and pulsed spontaneous parametric down-conversion sources under equivalent indistinguishability constraints and show that CW operation can achieve comparable rates while relaxing optical synchronization requirements.

In recent years, interest in photonic quantum technologies and quantum networks has grown rapidly. This progress drives demand for robust multi-photon quantum interference, an essential building block for measurement-device-independent quantum key distribution[1], boson sampling[2], photonic quantum repeaters[3], quantum teleportation[4], and entanglement swapping[5].

High-visibility quantum interference requires the interfering photons to be indistinguishable in all degrees of freedom[6,7]. The maximum achievable interference visibility between photons is bounded by the single-photon purity that is commonly engineered by tailoring the phase-matching condition and group velocities in nonlinear media[8–17] or by applying spectral filtering[18]. Beyond spectral considerations, temporal indistinguishability of photons must also be enforced. In the pulsed regime based on spontaneous parametric down-conversion (SPDC)[19–22], pair creation is confined to short pump pulses [Fig. 1 (a)]. The interference visibility in the pulsed regime depends on the single-photon wave packet duration and the precise synchronization of both the pump pulses and optical paths[23,24]. While this approach is well-suited to controlled laboratory settings, extending it to long-distance or distributed quantum networks requires active stabilization of emission times and path lengths across remote nodes, which are major challenges towards deployment in real network infrastructure[25].

An alternative approach, first proposed in ref. 5 and later demonstrated experimentally[26–28], employs photon sources pumped by continuous-wave (CW) lasers. In the CW regime, photon pairs are emitted randomly in time at a steady rate [Fig. 1(b)]. Temporal indistinguishability of photons is then enforced by post-selecting detection events within a narrow coincidence window τ_w satisfying $\tau_w \ll T_c$[27,29], where T_c denotes the coherence time of interfering photons. Physically, this corresponds to single-temporal-mode detection, in which the coincidence window acts as a temporal projector that selects indistinguishable emission events [Fig. 1c,d].

[1]Friedrich Schiller University Jena, Abbe Center of Photonics, Institute of Applied Physics, Jena, Germany. [2]Fraunhofer Institute for Applied Optics and Precision Engineering IOF, Jena, Germany. [3]Friedrich Schiller University Jena, Institute for Theoretical Physics, Jena, Germany. [4]Helmholtz Institute Jena, Jena, Germany. [5]National Institute of Information and Communications Technology (NICT), Tokyo, Japan. ✉e-mail: baghdasar.baghdasaryan@uni-jena.de; fabian.steinlechner@uni-jena.de

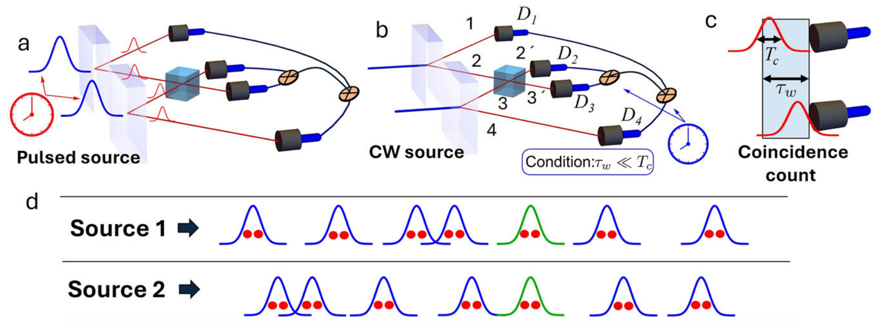

Fig. 1 | Temporal indistinguishability in pulsed and continuous-wave sources. **a** Realization of temporal indistinguishability between photons in entanglement swapping via time-synchronized pulsed photon sources. **b** Entanglement swapping with continuous-pumped photon pair sources. Temporally indistinguishable photons can be post-selected with single-photon detectors if the photon coherence time T_c exceeds the coincidence window τ_w of the detection events. **c** Detection of two photon-wave packets within a given coincidence window τ_w. Since the coincidence window is larger than the coherence time T_c, photon pairs with large temporal distances can be inaccurately counted as a simultaneous coincidence. **d** Continuous emission of photon pairs from two CW sources, where among all pairs, the temporally indistinguishable photons (green) can be post-selected.

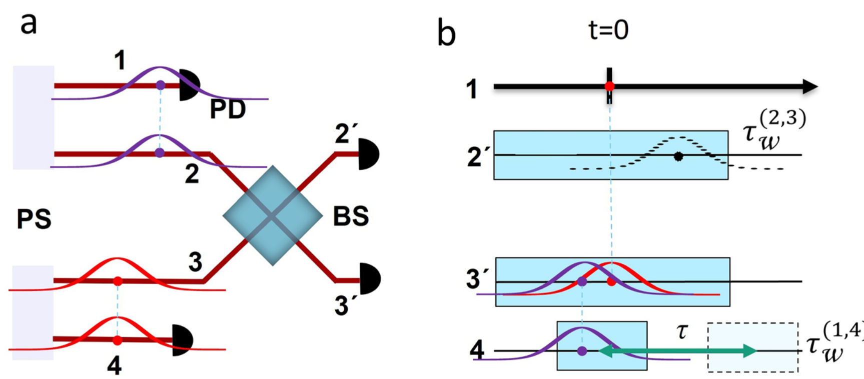

Fig. 2 | Coincidence-window selection in four-photon interference. **a** For explanatory purposes, we assume the outer photons are detected first. The coincidence window $\tau_w^{(1,4)}$ sets the maximum allowed time difference between the detection events in the spatial modes 1 and 4, if $j < \tau_w^{(1,4)}$ is ensured. Because of the strong time correlation within each pair, this $\tau_w^{(1,4)}$ window predetermines the temporal separation,and thus the indistinguishability of the photons in modes 2 and 3. The coincidence windows $\tau_w^{(2,3)}$ in spatial modes 2′ and 3′ do not affect this indistinguishability; they determine the probability of successfully capturing the wave packets of these photons. **b** The illustration of the coincidence windows relative to the trigger photon in the spatial mode 1. This example illustrates that the photons exit into the same spatial mode 3′, leaving 2′ empty. A noise photon (black dashed wave packet) can then occupy 2′ and produce a false four-fold. The dashed window in mode 4 indicates the τ-dependent shift of the $\tau_w^{(1,4)}$ coincidence window. BS: beam splitter; PD: photon detector; PS: photon-pair source.

Importantly, while the CW approach removes the requirement for optical synchronization of photon emission times, it does not eliminate the need for classical clock synchronization for the detection of correlated events. Instead, asynchronous CW operation shifts the synchronization task from optical emission-time control to electronic clock synchronization and post-selection, which is generally less demanding and easier to scale[30,31].

Despite the availability of highly coherent quantum light sources[32] and ultra-fast detectors[33] capable of accessing the single-temporal-mode regime[26], a quantitative design framework for the CW approach is still lacking. In particular, it remains unclear how strictly the condition $\tau_w \ll T_c$ needs to be satisfied in order to meet application-specific interference visibility thresholds–e.g., ≥50% for non-classical two-photon interference[34], ≥71% for Bell inequality violation[35], or ≥95% for cluster-state growth[36]. Moreover, the impact of finite detector timing jitter j on the indistinguishability of photons has not been analyzed quantitatively. These questions are central to assessing the scalability of asynchronous quantum networks driven by CW sources.

Here, we develop and experimentally validate a theoretical model that quantitatively describes photon indistinguishability in time-resolved Hong-Ou-Mandel (HOM) interference experiments in the CW SPDC regime[37–40]. We show that, in the low-noise limit, the HOM visibility is predominantly governed by the ratio T_c/τ_w. We verify this scaling experimentally using sources with different coherence times, without any post-hoc fitting. Based on this model, we analyze the attainable four-photon rates in a simple quantum-network scenario based on CW SPDC sources. We demonstrate that, for a given target visibility and fixed timing jitter j, an optimal coincidence window exists that maximizes the usable photon rate. Finally, we identify the parameter regime in which CW operation becomes advantageous for scalable quantum networks and compare its performance to pulsed SPDC sources under equivalent indistinguishability constraints.

Results

Multi-photon interference in the CW regime

We analyze a HOM-type multi-photon interference in the context of entanglement swapping, which is an essential protocol for quantum repeaters in global quantum networks[41–46]. A scheme of entanglement swapping in the CW regime is shown in Fig. 1b. Entanglement can be encoded in time[26,47–49], frequency[50], polarization[28,51,52], or orbital angular momentum[53]. Our subsequent analysis focuses exclusively on the temporal indistinguishability of photons, independent of the specific encoding degree of freedom.

Temporal indistinguishability is assessed through four-photon detection events in the setup shown in Fig. 2a. If photons in spatial modes 2 and 3 are indistinguishable and arrive simultaneously at the beam splitter (BS), they exit through the same output mode (2′ or 3′), which gives rise to the well-known HOM dip[23,24,54].

To describe this process theoretically, we begin with the biphoton states generated by two independent CW sources and then sequentially propagate the states through optical elements and apply detection operators. The results derived below apply to any photon-pair source operating in the CW regime. The biphoton state produced by a monochromatic CW source can be written as[55,56]

$$|\Psi\rangle_{i,k} = N\int d\Omega\, \Phi_{i,k}(\Omega)\, |\Omega\rangle_i |-\Omega\rangle_k, \tag{1}$$

where i and k denote the propagation modes, N is the normalization factor, Ω is the frequency deviation from the center frequency ω_0 ($\omega = \omega_0 \pm \Omega$). The biphoton mode function $\Phi_{i,k}(\Omega)$ describes the spectral structure of the source arising from the phase matching and dispersion.

For broadband sources, spectral filtering is required to extend the photon coherence time such that $\tau_w \ll T_c$. Narrowband filters are modeled as

$$\hat{\mathcal{F}}_i = \int d\Omega\, F_i(\Omega)\, |\Omega\rangle_i \langle\Omega|_i,$$

where $F_i(\Omega)$ denotes the filter transmission function. Applying this operator to the biphoton state yields

$$|\Psi\rangle_{i,k} \propto \int d\Omega\, J_{i,k}(\Omega)\, |\Omega\rangle_i |-\Omega\rangle_k, \tag{2}$$

where we introduced the following notation for the joint spectral amplitude:

$$J_{i,k}(\Omega) = F_i(\Omega)\, F_k(-\Omega)\, \Phi_{i,k}(\Omega).$$

Note that the spectral properties of the biphoton quantum state $|\Psi\rangle_{i,k}$ are primarily determined by the filter response if the filter bandwidth $F_i(\Omega)$ is much narrower than the intrinsic biphoton spectrum $\Phi_{i,k}(\Omega)$.

For two independent sources, the joint state of two photon pairs is

$$\begin{aligned}|\Psi\rangle_{1,2}|\Psi\rangle_{3,4} \propto &\iint d\Omega\, d\Omega'\, J_{1,2}(\Omega)\, J_{3,4}(\Omega') \\ &|\Omega\rangle_1 |-\Omega\rangle_2 |-\Omega'\rangle_3 |\Omega'\rangle_4.\end{aligned}$$

Next, we apply a 50/50 BS on the photons in modes 2 and 3 and retain only the terms in which the photons exit in different spatial modes. The resulting normalized state is given by

$$\begin{aligned}|\Psi\rangle_{1,2',3',4} \;=\;& N'\iint d\Omega\, d\Omega'\, J_{1,2}(\Omega)\, J_{3,4}(\Omega') \\ & |\Omega\rangle_1 |\Omega'\rangle_4 \left(|-\Omega\rangle_{2'}|-\Omega'\rangle_{3'} - |-\Omega'\rangle_{2'}|-\Omega\rangle_{3'}\right),\end{aligned} \tag{3}$$

where N' is the new normalization factor.

Photon detection at time t_0 with a perfect time resolution would be described by the projector $|t_0\rangle\langle t_0|$. In practice, finite detector timing resolution must be included through the normalized detector response function $g_i(t)$ [57]. We model the resulting measurement as the positive-operator-valued measure element

$$\hat{P}_i(t_0) = \int dt\, g_i(t) |t + t_0\rangle_i \langle t + t_0|_i. \tag{4}$$

Here, the detector efficiency is assumed to be unity and frequency independent. The response function $g_i(t)$ accounts for timing uncertainty arising from detector jitter j, which we model as a Gaussian with full width at half maximum (FWHM) j.

To express both the state from Eq. (3) and the detection operators in the same basis, we transform the detection operator into the frequency domain,

$$\hat{P}_i(t_0) = \iint d\Omega_1\, d\Omega_2\, g_{F,i}(\Omega_1 - \Omega_2)\, e^{it_0(\Omega_1-\Omega_2)} |\Omega_1\rangle_i \langle\Omega_2|_i, \tag{5}$$

where we used $a^\dagger(t) = \frac{1}{\sqrt{2\pi}}\int d\Omega\, a^\dagger(\Omega)\, e^{i\Omega t}$. The function $g_{F,i}(\Omega_1 - \Omega_2)$ is proportional to the Fourier transform of the detector response function

$$g_{F,i}(\Omega_1 - \Omega_2) = \frac{1}{2\pi}\int dt\, g_i(t)\, e^{it(\Omega_1-\Omega_2)}.$$

We now have all the components to describe the detection process. The probability that photons are detected at times t_1, t_2, t_3, t_4 is then

$$p(t_1, t_2, t_3, t_4) = \mathrm{Tr}\left(\hat{P}_1(t_1)\, \hat{P}_{2'}(t_2)\, \hat{P}_{3'}(t_3)\, \hat{P}_4(t_4)\, \rho\right),$$

where $\rho = |\Psi\rangle_{1,2',3',4}\langle\Psi|_{1,2',3',4}$ is the density operator of the composite system Eq. (3).

Next, we must include the finite coincidence windows used in the experiment. Photons in modes 1 and 4 serve as heralding (outer) photons, while photons in modes 2 and 3 interfere at the BS. The coincidence window between detections in modes 1 and 4 is denoted $\tau_w^{(1,4)}$ and defines the maximum allowed time difference between these detection events (assuming $j < \tau_w^{(1,4)}$). While earlier figures depict this as a graphical window in the coincidence histogram, in the following $\tau_w^{(1,4)}$ is treated as the time duration of the coincidence acceptance interval used to decide which events are counted as coincidences. A smaller $\tau_w^{(1,4)}$ therefore enforces tighter temporal synchronization. Due to strong time correlations within each photon pair, the coincidence window $\tau_w^{(1,4)}$ predetermines the temporal separation–and thus the indistinguishability–of the photons interfering in modes 2 and 3. In contrast, the coincidence windows $\tau_w^{(2,3)}$ applied in channels 2′ and 3′ only determine the probability of capturing the interfering wave packets and should therefore be chosen larger than the coherence time, $\tau_w^{(2,3)} > T_c$. In Fig. 2 b, the coincidence windows are presented by blue rectangles, where the photons in the spatial mode 1 are used for triggering.

To calculate the four-photon coincidence probability, we integrate over all detection times within the coincidence windows. All optical paths are assumed to be equal. The detection times of photons in modes 2′ and 3′ are set to the same and are integrated around a reference time $t = 0$ within $[-\tau_w^{(2,3)}/2, \tau_w^{(2,3)}/2]$. A variable arrival time τ is introduced for photons in the spatial mode 4 [see Fig. 2 b], to test how the HOM visibility changes when photons lose temporal overlap. This single-delay scan corresponds to the conventional HOM dip measurement. For given $\tau_w^{(1,4)}$, the highest interference is expected at $\tau = 0$ and no interference is expected at $\tau \gg T_c$. The integration range for t_4 is therefore $(\tau - \tau_w^{(1,4)}/2, \tau + \tau_w^{(1,4)}/2)$.

The integration over the coincidence windows for each value of τ yields:

$$\begin{aligned}\mathcal{P}(\tau) \;=\;& \int_{-\tau_w^{(2,3)}/2}^{\tau_w^{(2,3)}/2}\int_{-\tau_w^{(2,3)}/2}^{\tau_w^{(2,3)}/2} \\ & \int_{\tau-\tau_w^{(1,4)}/2}^{\tau+\tau_w^{(1,4)}/2} dt_2\, dt_3\, dt_4\, p(0, t_2, t_3, t_4).\end{aligned} \tag{6}$$

After applying the detection operators and evaluating the time integrals in Eq. (6), we end up with the following expression for the four-photon coincidence probability:

$$\begin{aligned}\mathcal{P}(\tau) \;=\;& d\Omega_1\, d\Omega_2\, d\Omega_3\, d\Omega_4\, \tau_w^{(1,4)} \\ & \times \mathrm{sinc}\left[\tfrac{\tau_w^{(1,4)}}{2}(\Omega_4 - \Omega_3)\right] \\ & \times J_{1,2}(\Omega_1)\, J^*_{1,2}(\Omega_2)\, J_{3,4}(\Omega_3)\, J^*_{3,4}(\Omega_4) \\ & \times g_{F,1}(\Omega_2 - \Omega_1) g_{F,4}(\Omega_4 - \Omega_3) e^{i\tau(\Omega_4-\Omega_3)} \\ & \times \left[\phi_2(\Omega_1, \Omega_2)\, \phi_3(\Omega_3, \Omega_4) + \phi_2(\Omega_3, \Omega_4)\, \phi_3(\Omega_1, \Omega_2)\right. \\ & \left.-\phi_2(\Omega_3, \Omega_2)\, \phi_3(\Omega_1, \Omega_4) - \phi_2(\Omega_1, \Omega_4)\, \phi_3(\Omega_3, \Omega_2)\right],\end{aligned} \tag{7}$$

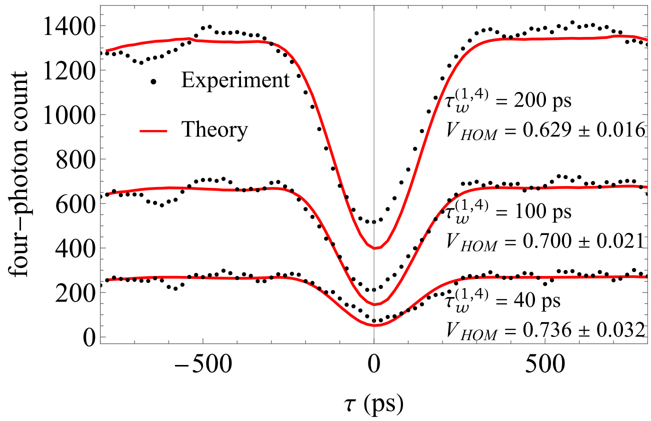

Fig. 3 | Time-resolved HOM dip for different coincidence windows. Black dots denote experimental data, and red solid curves denote theoretical predictions. The coincidence window of the photons in modes 2′ and 3′ is set to $\tau_w^{(2,3)} = 2000$ ps. For the theoretical calculation, we normalized Eq. (7) according to experimental photon count for $\tau_w^{(1,4)} = 40$ ps. The same normalization is used for the rest of the theoretical predictions. The total count was measured over a 1.5-h period. Uncertainties are defined as standard deviations.

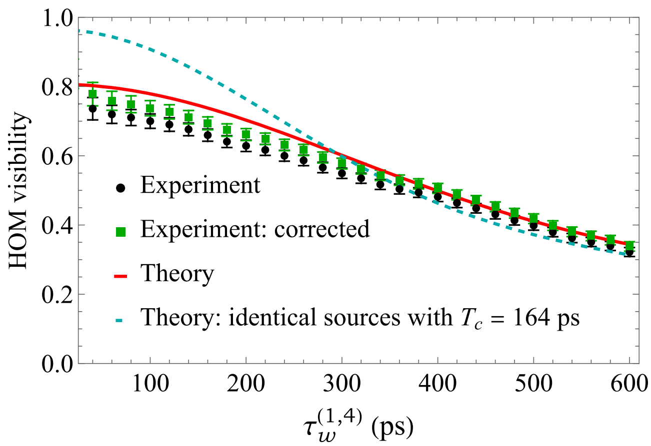

Fig. 4 | HOM visibility as a function of the coincidence window. The theoretical values (red solid curves) have been calculated with Eqs. (7) and (8) by using the parameters presented in Fig. 3. The black circles correspond to raw data, while the green squares represent the corrected HOM visibility after subtracting the accidental counts. The dashed blue line represents the theoretical calculation for the scenario where the two sources are identical with $T_{c,1} = T_{c,2} = 164$ ps. The theoretical prediction of HOM visibility in this scenario is 0.956 for $\tau_w^{(1,4)} = 40$ ps. Uncertainties are defined as standard deviations.

where

$$\phi_i(\Omega_1, \Omega_2) = \tau_w^{(2,3)} \operatorname{sinc}\left[\frac{\tau_w^{(2,3)}}{2}(\Omega_2 - \Omega_1)\right] g_{F,i}(\Omega_2 - \Omega_1).$$

Here, the *sinc* function arises from the convolution integral over the rectangular coincidence windows. The resulting expression for the four-photon coincidence probability $\mathcal{P}(\tau)$ depends on the delay τ, the coincidence windows $\tau_w^{(1,4)}$ and $\tau_w^{(2,3)}$, the detector timing jitter j, and the spectral filter response function.

HOM measurement

Figure 3 shows the measured and predicted four-photon coincidence count as a function of the detection delay in spatial mode 4 for several coincidence windows $\tau_w^{(1,4)}$. The coincidence windows between the trigger photon and the photons in modes 2′ and 3′ were chosen much larger than the photon coherence times, $\tau_w^{(2,3)} = 2000$ ps $\gg T_{c,1}, T_{c,2}$, such that temporal post-selection is governed solely by $\tau_w^{(1,4)}$. As the detection delay increases, the two-photon wave packets become temporally distinguishable, and the coincidence count rises, yielding the expected time-resolved HOM dip.

Red solid curves in Fig. 3 show the theoretical predictions obtained from Eq. (7). Detector timing jitters of $j = (17, 13, 11, 16)$ ps for modes 1-4 were used directly without post-hoc fitting; the only free scale parameter is a global normalization factor.

The theoretical probability $\mathcal{P}(\tau)$ was normalized to the experimental plateau at $\tau \gg T_c$ for the data with $\tau_w^{(1,4)} = 40$ ps after correction for accidental four-fold events (detailed in Supplementary Information) and subsequently applied to all theoretical curves. The model reproduces the measured HOM dips across all coincidence windows. The slightly elevated experimental offsets at larger $\tau_w^{(1,4)}$ are consistent with an increased contribution of accidental events.

All curves in Fig. 3 exhibit a HOM dip, yet retain a nonzero coincidence count at $\tau = 0$ due to imperfect interference visibility arising from residual photon distinguishability, due to a finite coincidence window, due to asymmetric filter functions, as well as accidental counts. To quantify the degree of indistinguishability of the photons in modes 2 and 3, we evaluate the HOM visibility

$$V_{HOM} = \frac{\mathcal{P}(\infty) - \mathcal{P}(0)}{\mathcal{P}(\infty)}, \tag{8}$$

where $\mathcal{P}(\infty)$ gives the probability of the coincidence measurement when the two wave packets are infinitely separated in time and do not interact. In practice, the time delay must be much larger than the photon's coherence time.

Figure 4 shows the measured (black dots) and predicted (red curve) HOM interference visibility as a function of $\tau_w^{(1,4)}$. There are two key observations. First, the visibility is below unity because the photons were partially distinguishable due to different coherence times of the two sources. A simulation for identical sources ($T_{c,1} = T_{c,2} = 164$ ps.) is shown for comparison (blue dashed curve). Second, the raw visibilities fall below the theoretical prediction because the theory assumes the emission of exactly two photon pairs, omitting higher-order pair emissions, stray photons, or dark counts. After subtracting the accidental coincidence contributions, which explicitly account for uncorrelated higher-order SPDC pair emissions, stray photons, and detector dark counts, the corrected visibilities (green squares) agree well with the theoretical prediction (see Supplementary Information for details on the quantification of accidental counts). This method assumes that the dominant additional photons are temporally uncorrelated with the selected pair events. Alternatively, instead of correcting the experimental data, these accidental contributions could be included in the theoretical model to reproduce the raw visibilities (black circles). While both approaches are fundamentally equivalent, we favor the subtraction method because incorporating all accidental-noise processes into the theory would require a comprehensive noise model for SPDC.

The very small remaining deviation between the theory and the corrected data may originate from the modeled filter response. Although the measured filter spectra were used in the calculation, the spectral phase was reconstructed using a transfer-matrix model of the fiber Bragg gratings (FBG) filters (see Methods for more details). In practice, the actual complex filter response may deviate from this idealized reconstruction.

Interplay among HOM visibility, coherence time, and timing jitter

Having validated the model against the four-fold-HOM measurements, we now use it to explore the parameter trade-offs governing CW interference. For this analysis, we consider identical sources with rectangular spectral filters and neglect accidental contributions in order to isolate effects arising from temporal distinguishability. We compute the HOM visibility as a function of coherence time T_c and coincidence window $\tau_w^{(1,4)}$ for fixed detector timing jitter.

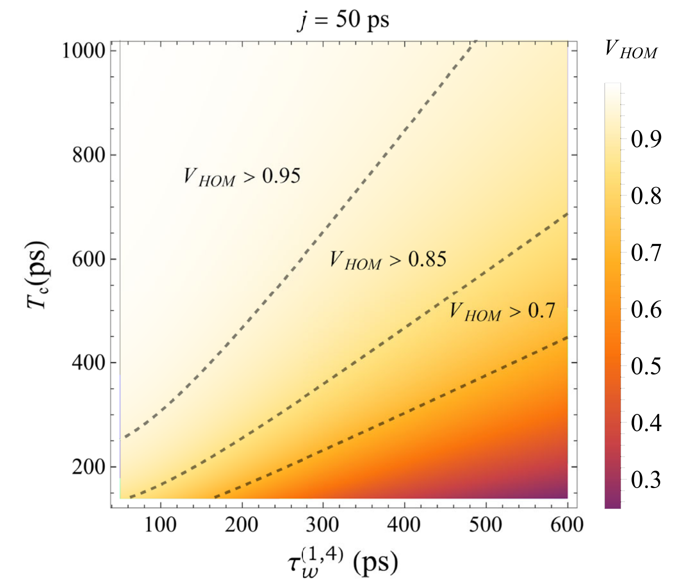

Fig. 5 | Coherence-time and coincidence-window scaling of HOM visibility. Theoretical calculation of HOM visibility is performed as a function of coherence time T_c and coincidence window $\tau_w^{(1,4)}$ for fixed timing jitter $j = 50$ ps. The color scale indicates V_{HOM}, and gray dashed lines mark fixed-visibility contours. The visibility is approximately constant for fixed ratios $T_c/\tau_w^{(1,4)}$. The deviation from linear behavior at short timescales arises from the finite timing jitter.

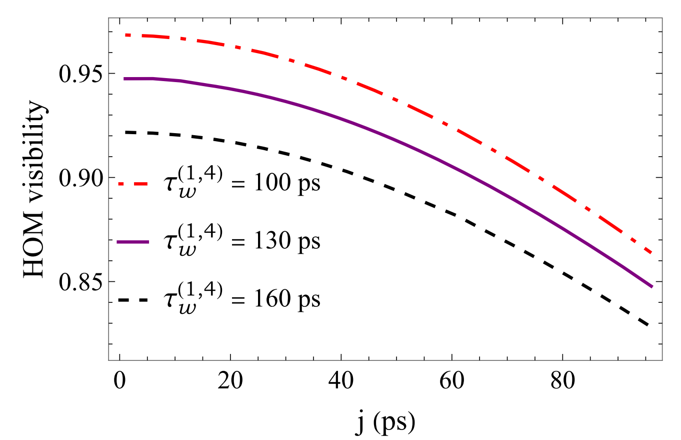

Fig. 6 | Detector-jitter dependence of HOM visibility. Theoretical calculation of HOM visibility as a function of the timing jitter j for different coincidence windows $\tau_w^{(1,4)}$. A rectangular filter function was applied, which results in a coherence time of 285 ps for both sources. The visibility can be increased by decreasing the timing jitter. The accidental counts are not included in this calculation.

Figure 5 shows that, for a given target HOM visibility, the scaling is primarily determined by the ratio $T_c/\tau_w^{(1,4)}$, with small deviation at small timescales arising from finite timing jitter. For example, achieving $V_{HOM} = 0.95$ requires $T_c/\tau_w^{(1,4)} \gtrsim 3.5$ for coherence times up to 250 ps, while visibilities around 0.85 are obtained already for $T_c/\tau_w^{(1,4)} \approx 1$. In practice, this ratio must be chosen more conservatively to mitigate the impact of accidental coincidences.

We reiterate that the method for estimating the HOM visibility shown in Fig. 2 (i.e., the condition $\tau_w^{(2,3)} \gg T_c$) evaluates the on-demand HOM visibility of the heralded photons in modes 2 and 3. This estimation relies exclusively on the temporal filtering of the heralding photons in modes 1 and 4 (for a more detailed explanation, see the Supplementary Information). The HOM visibility can be further improved by applying temporal filtering to photons 2 and 3 as well (i.e., using narrow coincidence windows)[40]. Doing so allows the required ratio $T_c/\tau_w^{(1,4)}$ for a given target HOM visibility to be relaxed by up to a factor of two. However, a different method must be applied to estimate the HOM visibility in this regime. A detailed discussion of that calibration procedure will be provided in a follow-up work.

In an entanglement swapping experiment, the roles of heralding and heralded photons are reversed: the coincidence detection of photons in modes 2′ and 3′ (the Bell state measurement) heralds the entangled state in modes 1 and 4. Consequently, the coincidence window $\tau_w^{(2,3)}$ must be narrow, while $\tau_w^{(1,4)}$ can remain wide.

Beyond optimization of the coincidence window, HOM visibility can be enhanced by decreasing timing jitter. Figure 6 shows the theoretical HOM visibility as a function of timing jitter j for different coincidence windows, where both sources possess a coherence time of 285 ps. While decreasing j systematically improves the visibility, a finite upper bound remains for each coincidence window. This limit arises from residual temporal distinguishability introduced by the finite coincidence window.

Rate-visibility trade-off

The preceding analysis shows that achieving high HOM visibility requires reducing the coincidence window. This improves temporal indistinguishability but simultaneously reduces the number of usable events. Here, we use τ_w as a generic notation for the relevant coincidence windows.

A key limitation of SPDC sources is the multi-pair emission, i.e., the generation of more than one photon pair per source within a single coherence time T_c[58]. Suppressing this noise requires operation in the photon-starved regime $\mu \ll 1$, where μ denotes the mean number of generated pairs per pump pulse for pulsed operation, or per coherence time for CW operation. A typical choice is $\mu \approx 0.01$. In the CW regime, the effective temporal mode rate is set by $1/T_c$, and the average pair-generation rate of a single source is therefore μ/T_c. Here, T_c is the coherence time of identical sources.

Entanglement swapping with independent CW sources requires that both sources emit a pair within the same coincidence window τ_w. The probability that a source emits a pair inside this window is $\mu\,\tau_w/T_c$. For two identical and independent sources, the probability that both emit a pair within the same window is therefore $(\mu\tau_w/T_c)^2$. Dividing by the window duration τ_w therefore yields the corresponding four-photon coincidence rate,

$$R = \left(\frac{1}{T_c}\mu\right)^2 \tau_w. \tag{9}$$

Equation (9) describes the obtainable four-photon rate in the absence of transmission and detection loss.

We now use this scaling to determine the coincidence window that maximizes the usable four-photon rate for a given target HOM visibility. Figure 7 shows the maximal four-photon rates as a function of the coincidence window τ_w for different detector timing jitters. For each point, the coherence time is adjusted to maintain the target HOM visibility. The coherence time is limited to 800 ps to remain within realistic source parameters. We set the mean photon number to $\mu = 0.01$, ensuring low multi-pair contributions. An optimal coincidence window clearly emerges for each jitter value, demonstrating that the usable rate can be maximized by jointly choosing τ_w and T_c for a desired HOM visibility. Figure 8 shows the same optimization for fixed timing jitter and varying target visibility, where we notice that a reduction of the target visibility can drastically increase the maximum detection rate.

Comparison of pulsed and CW regimes

It is instructive to compare the timing constraints governing indistinguishability of photons in pulsed and CW SPDC sources. This comparison is intended as an order-of-magnitude scaling estimate under matched indistinguishability constraints.

In the pulsed regime, photon-pair creation is confined to a pump pulse of duration τ_p, while consecutive pulses are separated by the inverse

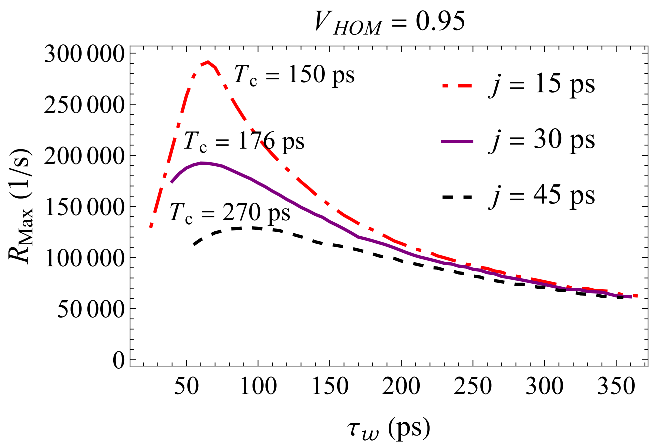

Fig. 7 | Maximum four-photon rate at fixed HOM visibility. Maximum achievable four-photon rate per second is evaluated as a function of coincidence window for various timing jitters and for a fixed HOM visibility $V_{HOM} = 0.95$. We observe that a reduction in timing jitter allows us to reach a higher photon rate. The coherence time is varied with τ_w to maintain the required HOM visibility; the depicted coherence times T_c correspond to values at which the rates are maximized.

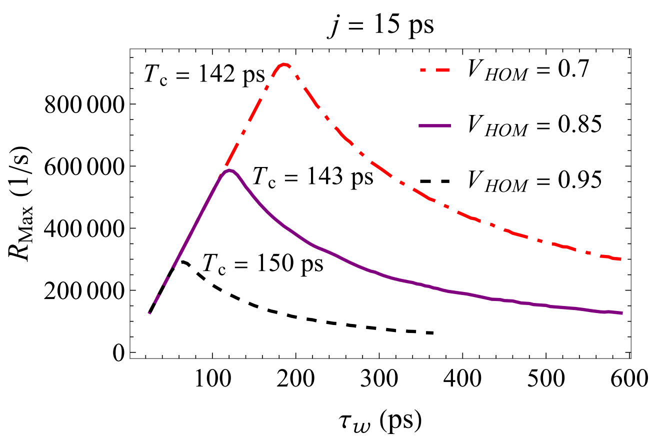

Fig. 8 | Visibility-dependent optimization of four-photon rates. Same as Fig. 7, but presented for various HOM visibilities and for fixed timing jitter $j = 15$ ps. There is an optimal size of τ_w for each V_{HOM}, which maximizes the four-photon rate. The depicted T_c values correspond to values at which the rates are maximized.

repetition rate $1/f_{\text{rep}}$. To avoid cross-talk between neighboring pulses, the coincidence window must satisfy $\tau_w \lesssim 1/f_{\text{rep}}$. Moreover, the single-photon coherence time T_c should be comparable to or exceed the pump pulse duration τ_p to suppress timing distinguishability within a pulse[59]. Therefore, the pulse synchronization addresses inter-pulse alignment, whereas the ratio τ_p/T_c addresses intra-pulse temporal-mode indistinguishability. Both are required for high HOM visibility. Under indistinguishability constraints comparable to those in the CW case, the per-pulse four-photon probability scales as $(\mu_p\tau_p/T_c)^2$, where μ_p is the per-pulse probability to generate a photon pair. Multiplication of the four-photon probability by the repetition rate yields the four-photon coincidence rate

$$R_{\text{pulsed}} \approx (\mu_p\tau_p/T_c)^2 f_{\text{rep}}, \tag{10}$$

up to constant factors such as Bell-state measurement efficiency and transmission or detection losses.

Here, two primary comparisons between the pulsed and CW regimes are necessary: achievable indistinguishability and generation rates. First, as we can see from the comparison of Eqs. (9) and (10), the ratios T_c/τ_w and T_c/τ_p play analogous roles as parameters controlling intra-window or intra-pulse temporal-mode indistinguishability. As shown in Fig. 5, achieving HOM visibilities exceeding 90% in the CW regime requires the ratio T_c/τ_w to be approximately greater than 1.5. A comparable ratio of the coherence time to the pulse duration, T_c/τ_p, is experimentally accessible in the pulsed regime. Note, however, that in the pulsed regime, temporal single-mode operation is typically achieved through engineering the phase-matching function, e.g., through apodized poling of the nonlinear material[13] rather than spectral filtering.

Second, the effective temporal mode rates are determined by f_{rep} and $1/\tau_w$ in the pulsed and CW regimes, respectively. GHz-class pulsed laser and SPDC source platforms relevant for high-rate photonic interference protocols have been demonstrated[60–63]. For repetition rates between 1 GHz to 50 GHz systems, the temporal separation between pulses ranges from 1 ns down to 20 ps. Coincidence windows of this duration are within the reach of state-of-the-art timing systems, a capability we also leveraged in our experiment. Therefore, by employing comparable temporal selection criteria, the achievable four-photon rates in the pulsed and CW regimes become comparable.

The key distinction, however, is that CW operation removes the need for optical emission-time and path-length stabilization between independent sources. Instead, only electronic time-stamping, classical clock synchronization, and postprocessing are required, shifting the synchronization burden from the optical to the electronic domain, which is considerably less demanding.

Overall, CW operation trades a reduction in maximum achievable rate for a substantial relaxation of optical path matching requirements. This trade-off might become favorable for long-distance quantum networking, where stabilizing optical paths between independent photon sources is technically demanding, in particular in the context of satellite links. In practice, the spectral filtering required to reach long coherence times can introduce significant additional optical loss, which further motivates the development of intrinsically narrowband or spectrally engineered photon-pair sources.

Application to long-distance quantum-network links

We now estimate entanglement-swapping rates for long-distance quantum-network links, with particular emphasis on satellite-based scenarios. In such networks, optical synchronization of independent photons at a beam splitter becomes increasingly challenging because path-length fluctuations, atmospheric turbulence, and satellite motion have to be controlled simultaneously. In a pulsed implementation, the arrival times of the photons have to be synchronized to within their coherence time, typically on the sub-picosecond to few-picosecond scale. The asynchronous CW approach, where photon pairs are generated at random times, and indistinguishability is recovered a posteriori by selecting temporally single-mode coincidence events, relaxes this requirement and is therefore particularly well suited to this regime.

Including transmission and detection efficiencies η_i, the expected four-photon coincidence rate is

$$R = \left(\frac{1}{T_c}\mu\right)^2 \tau_w \times \frac{1}{2} \times \eta_1\eta_2\eta_3\eta_4, \tag{11}$$

where the factor 1/2 accounts for the intrinsic success probability of linear-optical Bell-state measurements. Throughout the simulation, we assume $\mu = 0.01$, a coherence time of T_c = 350 ps and a coincidence window of τ_w = 100 ps. According to Fig. 5, this parameter regime should allow high HOM visibility, with $V > 0.95$.

As a concrete high-loss example, we consider a configuration where photons 2 and 3 from two distant sources are interfered on a beam splitter. For the long-distance segments, we consider losses of 23 dB per channel, which is comparable to those of a low-Earth-orbit (LEO) satellite or approximately 100 km of low-loss fiber transmission and an additional fiber loss of 2.2 dB corresponding to approximately 10 km of additional SMF for photons 1 and 4.

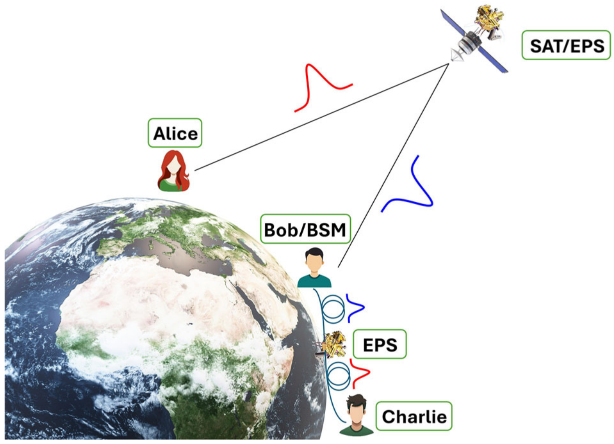

Fig. 9 | Asynchronous entanglement swapping in a satellite-assisted (SAT) quantum network. Entanglement swapping with a Bell-state measurement (BSM) performed at a ground station. Entangled photon pairs are generated by a space-based entangled photon source (EPS) onboard a satellite and by a ground-based EPS, while the BSM links free-space and fiber segments. The satellite EPS operates in the CW regime and emits photon pairs at random times; temporal indistinguishability is obtained by temporally single-mode coincidence analysis at the ground station.

With these parameters, we obtain with Eq. (11) approximately one successful entanglement-swapping event every 2.7 s. For the same loss values and under the same high-visibility condition, $T_c/\tau_p \simeq T_c/\tau_w \simeq 3.5$, a pulsed source operated at a typical repetition rate of 80 MHz would yield one successful swap every 335 s. As previously discussed, higher swapping rates for the pulsed regime are achievable with increased $f_{\rm rep}$ of the pump, and would again be comparable to the CW regime for $f_{\rm rep}$ in GHz range.

We further extend the analysis to realistic satellite passes for a single low-Earth-orbit satellite. An entangled-photon source onboard the satellite distributes photons to ground stations, where one of the photons interferes with a photon from a terrestrial fiber network in a BSM. The geometry is shown in Fig. 9. Assuming the sender and receiver telescope parameters, adaptive-optics performance, atmospheric-turbulence model, and pointing-and-tracking parameters stated in ref. 64, we simulate the downlink losses at $\lambda = 1550$ nm. We consider simultaneous access between two ground stations located in Paris and Berlin. The satellite orbit is chosen to match the Micius mission[65]. We assume an additional terrestrial fiber segment of 10 km from the ground-based entangled-photon source to Bob and Charlie, corresponding to a loss of 2.2 dB.

For each satellite pass, we integrate Eq. (11) over the time-dependent channel transmission. The losses for the median pass vary between approximately 30 dB and 24 dB during the acquisition window. With the parameters stated above, we find a total of 1745 successful entanglement-swapping events over one year, distributed over 316 simultaneous-access passes. The median number of successful swaps is 5 events per pass.

The resulting rates remain modest, as expected in this strongly loss-dominated regime. Substantial improvements can be expected from spectral, spatial, or temporal multiplexing; from sources operated at an optimized trade-off between pair probability and visibility; from improved coupling and adaptive-optics performance; further advances in low-jitter, high-efficiency single-photon detectors, and deterministic photon sources. In addition, satellite constellations or multiple orbital planes would increase the number of simultaneous-access windows and therefore the annual number of usable swapping events.

In the scheme shown in Fig. 9, the propagation delays from the satellite to the ground stations must still be estimated in order to identify the correct coincidence events; however, this can be handled by classical clock synchronization and time-tag post-processing. The relevant alternative in a pulsed implementation is optical synchronization of independent photons at the beam splitter with comparable, or even smaller, timing uncertainty, typically set by the photon coherence time or pulse duration. This requirement is even more demanding from an experimental and operational perspective. The asynchronous CW approach, therefore, does not eliminate the need for precise timing, but shifts the requirement from real-time optical arrival-time synchronization to high-resolution time tagging.

Several important factors are not included in this discussion. In particular, Doppler shifts, polarization rotations, atmospheric dispersion, background counts, and the detailed implementation of clock recovery and time tagging must be treated in more detail. These aspects are beyond the scope of the present study.

Discussion

We developed and experimentally validated a theoretical framework that quantitatively describes multi-photon interference in the CW SPDC regime. The model incorporates detector timing jitter j, photon coherence time T_c, and the coincidence window τ_w into an effective description of temporal indistinguishability. The framework provides a consistent procedure to estimate HOM visibility in asynchronous applications, particularly relevant to long-distance quantum communication networks.

Using this framework, we identified the scaling laws governing time-resolved HOM interference. We showed that the achievable visibility is primarily determined by the ratio T_c/τ_w. Finite detector timing jitter introduces additional deviations at short timescales, but the dominant design parameter remains the temporal-mode selectivity set by filtering and coincidence-window selection.

These insights translate into practical design rules for asynchronous quantum networking. For a given target visibility and fixed timing jitter, an optimal coincidence window exists that maximizes the usable four-photon rate. Comparison with pulsed SPDC sources shows that CW operation can achieve comparable rates while removing the need for precise optical emission-time synchronization between independent sources. This relaxation of synchronization requirements makes the CW approach particularly attractive for real-world long-distance quantum networks.

At the same time, CW operation does not remove the need for precise timing in general. Rather, it changes the problem from optical synchronization of photon wave packets to stable clock alignment and high-resolution coincidence analysis. This distinction is particularly relevant for satellite-based quantum networks, where electronic synchronization is challenging, but still experimentally more tractable than optical synchronization at comparable, or even smaller, timing uncertainty budgets. A detailed comparison between pulsed and CW operation will require a system-level optimization that includes source brightness, photon coherence time, detector jitter, time-tagging resolution, clock stability, channel loss, and the target interference visibility. Identifying protocol-specific trade-offs and optimal operating points for a given synchronization budget remains an important challenge for future work.

Methods

Experimental setup

The experimental setup shown in Fig. 10 consists of a 775 nm pump laser obtained by second-harmonic generation from a continuous-wave laser at 1550 nm using a fiber-coupled, periodically poled lithium niobate (ppLN) waveguide. The pump laser is split using a fiber polarizing beam splitter (PBS) to drive SPDC emission in two separate ppLN waveguides. The waveguides generate correlated photons centered at 1550 nm via type-0 SPDC. Each waveguide is mounted on an independent temperature-stabilized stage with a stability of ±0.01 °C. Signal and idler photons are separated using wavelength-division multiplexers and spectrally filtered with FBGs. The filters include femtosecond-inscribed in-house devices[66] and commercial FBGs (Teraxion). The transmission spectra of the FBGs have a FWHM of 27 pm and 41 pm for the idlers and 41 pm and 44 pm for signals. To erase polarization distinguishability, the photons are coupled into a fiber PBS, and their polarization is optimized using fiber polarization controllers. The idler photons are then interfered on a 50/50 BS. We note that placing the idler filters downstream of the 50/50 BS would suppress which-path information associated with different filter widths and is

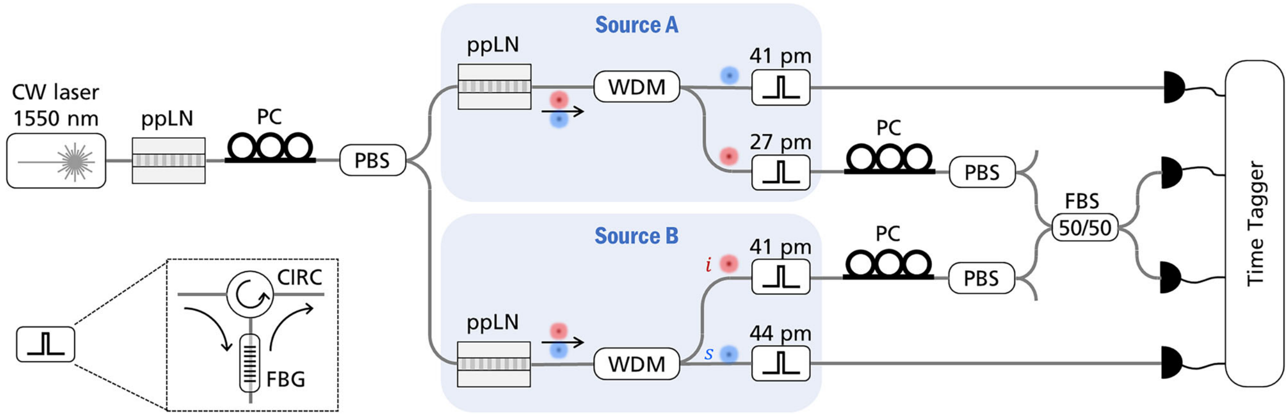

Fig. 10 | Experimental setup for performing four-photon HOM interference. A CW telecom laser is up-converted and then split into two paths to pump two SPDC sources, A and B (blue boxes). The generated two-photon states are separated with a wavelength division multiplexer (WDM) according to their higher or lower frequencies, followed by tight filtering with a fiber Bragg grating, as described in the left inset. The signal photons (blue) are used to herald the interference, while the idler photons (red) are interfered at a polarization-maintaining fiber beam splitter (FBS). CIRC: circulator; PBS: polarization beam splitter; PC: polarization controller; ppLN: periodically-poled lithium niobate waveguide.

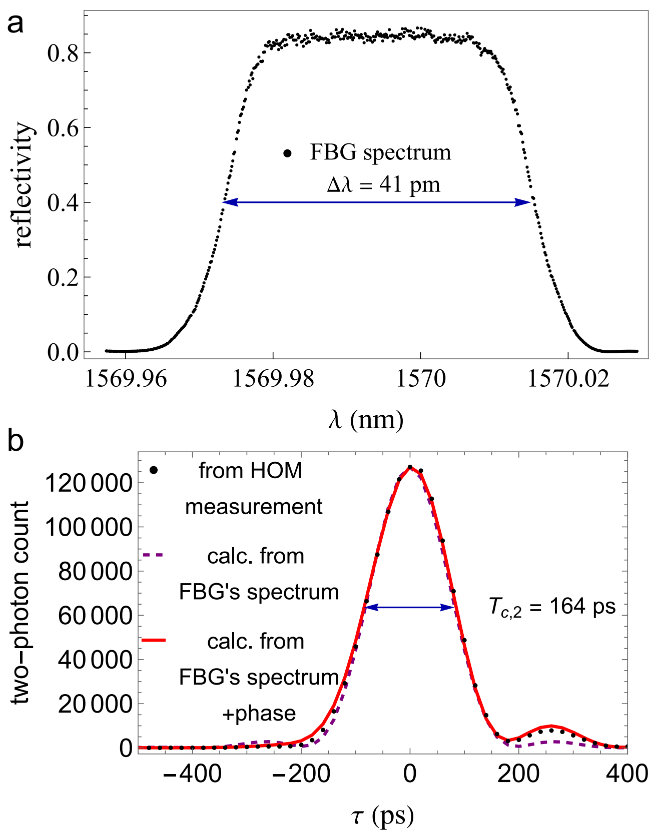

Fig. 11 | Biphoton coherence function from fiber Bragg grating filters. **a** Normalized reflection spectrum of the fiber Bragg gratings (FBG) filter with a bandwidth of $\Delta\lambda = 41$ pm. The wavelength-dependent reflectance was determined by normalizing the reflected signal to the incident probe spectrum. **b** Two-photon coincidence count for the source B (black dots) compared with the calculated (calc.) and normalized coherence function without (dashed purple curve) and with the phase model (solid red curve). Asymmetry in τ is attributed to the wavelength-dependent phase response of the FBG filters.

therefore the preferable configuration in high-visibility entanglement-swapping experiments. In the present implementation, the filters were positioned before the BS, whereby different filter bandwidths enabled benchmarking the observed experimental imperfections against the theoretical model.

All four photons were detected using superconducting nanowire single photon detectors (SNSPD, Single Quantum). Detection events are recorded by a time-tagging unit (quTools) with a root-mean-square timing jitter of 4.2 ps. In the theoretical analysis, the overall temporal response is modeled as the convolution of the time-tagger and detector timing jitters.

Temporal coherence function of biphoton state

Here, we experimentally characterize the temporal coherence of the generated photon pairs. The temporal coherence of the biphoton wave packet is determined by the spectral amplitude and phase of the applied FBG filters. Figure 11a shows the reflected power spectrum of $\Delta\lambda = 41$ pm FBG filter obtained by an optical spectrum analyzer. Since this measurement provides only the spectral magnitude, we reconstruct the spectral phase using a transfer-matrix model of the FBG[67]. A super-Gaussian refractive-index profile is assumed, and its parameters are optimized to reproduce the measured reflection spectrum. The spectral phase is then extracted from the resulting complex transfer function.

The temporal coherence function is obtained from Eq. (2) by applying the detection operators Eq. (5) on signal and idler photons with relative time delay τ:

$$\begin{aligned} G_{i,k}(\tau) \quad = \quad & \iint d\Omega_1\, d\Omega_2\, J_{i,k}(\Omega_1)\, J^*_{i,k}(\Omega_2)\, e^{i(\Omega_1-\Omega_2)\tau} \\ & \times g_{F,i}(\Omega_2-\Omega_1)\, g_{F,k}(\Omega_1-\Omega_2). \end{aligned}$$

This function represents the probability density of detecting an idler photon at time delay τ relative to the signal photon.

Figure 11b compares the measured two-photon coincidences of the source B with the calculated temporal coherence function. Including the reconstructed spectral phase (solid red curve) reproduces the experimentally observed side peak, whereas a phase-free model (dashed purple curve) fails to capture this feature. The asymmetry in τ arises from the wavelength-dependent phase response of the FBG filters. Both experiment and theory yield approximately a coherence time of $T_{c,2} = 164$ ps defined as FWHM. The same procedure yields $T_{c,1} = 244$ ps for the source A. Consistency is confirmed by computing the coherence function directly from Eq. (7) by tracing over the arrival times of the remaining photons, i.e., assuming infinitely large coincidence windows. The asymmetric filter configuration was the closest matching pair of filters available. While not optimal from a performance perspective, the configuration does allow us to test the theoretical model in a more general and experimentally realistic situation with unequal filter bandwidths and different coherence times.

Accidental-coincidence correction

The raw four-photon counts contain contributions from genuine two-pair events as well as accidental coincidences. The latter originate mainly from uncorrelated higher-order SPDC emissions, stray photons, and detector dark counts within the applied coincidence windows. In the low-gain regime considered here, events involving four fully uncorrelated photons are negligible. The dominant accidental contributions contain one genuine photon pair together with two noise photons.

We estimate this accidental background directly from the recorded time tags. To this end, the genuine pairwise timing correlations are deliberately broken by adding a constant temporal offset Δ to all detections in one of the beam-splitter output channels, chosen much larger than the coincidence window $\tau_w^{(2,3)}$. When the time tags of channel $2'$ are shifted, any remaining four-photon coincidence must contain an accidental count in that channel. The same procedure is then repeated by shifting channel $3'$. The corrected four-photon probability is obtained by subtracting the two shifted contributions $A_{s,2'}$ and $A_{s,3'}$ from the raw four-photon rate

$$A_0 - A_{s,2'} - A_{s,3'},$$

where A_0 is the total recorded four-fold rate at zero delay. The estimation of corrected four-fold at large delay is conducted in a similar manner.

This shifted-window method works well in the low-noise regime considered here. In a higher-gain regime, temporally correlated multi-pair contributions may become more relevant, and a complete treatment would require a full theoretical noise model for CW SPDC. We leave such an analysis for future work.

This procedure does not require additional measurements, since the accidental background is estimated from the same time-tag dataset. In an actual entanglement-swapping experiment, however, this subtraction is generally not available in real time. A detailed probability-level description of the shifted-window correction is provided in the Supplementary Information.

Data availability

The datasets generated and/or analyzed during the current study are not publicly available because they contain raw time-tag data and analysis files that are not part of a public repository, but are available from the corresponding author on reasonable request.

Code availability

The code used to analyze the data and generate the results of the current study is available from the corresponding author on reasonable request.

Received: 5 March 2026; Accepted: 16 July 2026;
Published online: 30 July 2026

References

1. Wang, W., Tamaki, K. & Curty, M. Measurement-device-independent quantum key distribution with leaky sources. *Sci. Rep.* **11**, 1678 (2021).
2. van der Meer, R., Renema, J. J., Brecht, B., Silberhorn, C. & Pinkse, P. W. H. Optimizing spontaneous parametric down-conversion sources for boson sampling. *Phys. Rev. A* **101**, 063821 (2020).
3. Azuma, K., Tamaki, K. & Lo, H.-K. All-photonic quantum repeaters. *Nat. Commun.* **6**, 6787 (2015).
4. Ren, J.-G. et al. Ground-to-satellite quantum teleportation. *Nature* **549**, 70–73 (2017).
5. Żukowski, M., Zeilinger, A., Horne, M. A. & Ekert, A. K. "event-ready-detectors" bell experiment via entanglement swapping. *Phys. Rev. Lett.* **71**, 4287–4290 (1993).
6. Qian, K. et al. Multiphoton non-local quantum interference controlled by an undetected photon. *Nat. Commun.* **14**, 1480 (2023).
7. Wang, K. et al. Entangling independent particles by path identity. *Phys. Rev. Lett.* **133**, 233601 (2024).
8. Grice, W. P., U'Ren, A. B. & Walmsley, I. A. Eliminating frequency and space-time correlations in multiphoton states. *Phys. Rev. A* **64**, 063815 (2001).
9. Garay-Palmett, K. et al. Photon pair-state preparation with tailored spectral properties by spontaneous four-wave mixing in photonic-crystal fiber. *Opt. Express* **15**, 14870–14886 (2007).
10. Brańczyk, A. M., Fedrizzi, A., Stace, T. M., Ralph, T. C. & White, A. G. Engineered optical nonlinearity for quantum light sources. *Opt. Express* **19**, 55–65 (2011).
11. Dixon, P. B., Shapiro, J. H. & Wong, F. N. C. Spectral engineering by gaussian phase-matching for quantum photonics. *Opt. Express* **21**, 5879–5890 (2013).
12. Mosley, P. J. et al. Heralded generation of ultrafast single photons in pure quantum states. *Phys. Rev. Lett.* **100**, 133601 (2008).
13. Dosseva, A., Cincio, L. & Brańczyk, A. M. Shaping the joint spectrum of down-converted photons through optimized custom poling. *Phys. Rev. A* **93**, 013801 (2016).
14. Tambasco, J.-L., Boes, A., Helt, L. G., Steel, M. J. & Mitchell, A. Domain engineering algorithm for practical and effective photon sources. *Opt. Express* **24**, 19616–19626 (2016).
15. Graffitti, F., Barrow, P., Proietti, M., Kundys, D. & Fedrizzi, A. Independent high-purity photons created in domain-engineered crystals. *Optica* **5**, 514–517 (2018).
16. Pickston, A. et al. Optimised domain-engineered crystals for pure telecom photon sources. *Opt. Express* **29**, 6991–7002 (2021).
17. Baghdasaryan, B., Steinlechner, F. & Fritzsche, S. Enhancing the purity of single photons in parametric down-conversion through simultaneous pump-beam and crystal-domain engineering. *Phys. Rev. A* **108**, 023718 (2023).
18. Blay, D. R., Steel, M. J. & Helt, L. G. Effects of filtering on the purity of heralded single photons from parametric sources. *Phys. Rev. A* **96**, 053842 (2017).
19. Pan, J.-W., Bouwmeester, D., Weinfurter, H. & Zeilinger, A. Experimental entanglement swapping: entangling photons that never interacted. *Phys. Rev. Lett.* **80**, 3891–3894 (1998).
20. Jennewein, T., Weihs, G., Pan, J.-W. & Zeilinger, A. Experimental nonlocality proof of quantum teleportation and entanglement swapping. *Phys. Rev. Lett.* **88**, 017903 (2001).
21. Yang, T. et al. Experimental synchronization of independent entangled photon sources. *Phys. Rev. Lett.* **96**, 110501 (2006).
22. Jin, R.-B., Takeoka, M., Takagi, U., Shimizu, R. & Sasaki, M. Highly efficient entanglement swapping and teleportation at telecom wavelength. *Sci. Rep.* **5**, 9333 (2015).
23. Hong, C. K., Ou, Z. Y. & Mandel, L. Measurement of subpicosecond time intervals between two photons by interference. *Phys. Rev. Lett.* **59**, 2044–2046 (1987).
24. Drago, C. & Brańczyk, A. M. Hong–ou–mandel interference: a spectral–temporal analysis. *Can. J. Phys.* **102**, 411–421 (2024).
25. Sun, Q.-C. et al. Quantum teleportation with independent sources and prior entanglement distribution over a network. *Nat. Photonics* **10**, 671–675 (2016).
26. Halder, M. et al. Entangling independent photons by time measurement. *Nat. Phys.* **3**, 692–695 (2007).
27. Halder, M. et al. High coherence photon pair source for quantum communication. *N. J. Phys.* **10**, 023027 (2008).
28. Tsujimoto, Y. et al. High-fidelity entanglement swapping and generation of three-qubit ghz state using asynchronous telecom photon pair sources. *Sci. Rep.* **8**, 1446 (2018).
29. Huang, Y.-P., Altepeter, J. B. & Kumar, P. Heralding single photons without spectral factorability. *Phys. Rev. A* **82**, 043826 (2010).
30. Spiess, C. et al. Clock synchronization with correlated photons. *Phys. Rev. Appl.* **19**, 054082 (2023).

31. Spiess, C. & Steinlechner, F. Clock synchronization with pulsed single photon sources. *Quantum Sci. Technol.* **9**, 015019 (2023).
32. Samara, F. et al. High-rate photon pairs and sequential time-bin entanglement with Si_3N_4 microring resonators. *Opt. Express* **27**, 19309–19318 (2019).
33. Natarajan, C. M., Tanner, M. G. & Hadfield, R. H. Superconducting nanowire single-photon detectors: physics and applications. *Superconductor Sci. Technol.* **25**, 063001 (2012).
34. Moschandreou, E. et al. Experimental study of Hong–Ou–Mandel interference using independent phase randomized weak coherent states. *J. Lightwave Technol.* **36**, 3752–3759 (2018).
35. Vértesi, T. More efficient Bell inequalities for Werner states. *Phys. Rev. A* **78**, 032112 (2008).
36. Chan, M. L. et al. Tailoring fusion-based photonic quantum computing schemes to quantum emitters. *PRX Quantum* **6**, 020304 (2025).
37. Legero, T., Wilk, T., Kuhn, A. & Rempe, G. Time-resolved two-photon quantum interference. *Appl. Phys. B* **77**, 797–802 (2003).
38. Legero, T., Wilk, T., Hennrich, M., Rempe, G. & Kuhn, A. Quantum beat of two single photons. *Phys. Rev. Lett.* **93**, 070503 (2004).
39. Legero, T., Wilk, T., Kuhn, A. & Rempe, G. Characterization of single photons using two-photon interference. **53** of *Advances in Atomic, Molecular, and Optical Physics*, 1-466. https://www.sciencedirect.com/science/article/pii/S1049250X06530095 (Academic Press, 2006).
40. Tsujimoto, Y. et al. High-visibility Hong-Ou-Mandel interference via a time-resolved coincidence measurement. *Opt. Express* **25**, 12069–12080 (2017).
41. Briegel, H.-J., Dür, W., Cirac, J. I. & Zoller, P. Quantum repeaters: the role of imperfect local operations in quantum communication. *Phys. Rev. Lett.* **81**, 5932–5935 (1998).
42. Duan, L.-M., Lukin, M. D., Cirac, J. I. & Zoller, P. Long-distance quantum communication with atomic ensembles and linear optics. *Nature* **414**, 413–418 (2001).
43. Zhao, Z., Yang, T., Chen, Y.-A., Zhang, A.-N. & Pan, J.-W. Experimental realization of entanglement concentration and a quantum repeater. *Phys. Rev. Lett.* **90**, 207901 (2003).
44. Goebel, A. M. et al. Multistage entanglement swapping. *Phys. Rev. Lett.* **101**, 080403 (2008).
45. Liao, S.-K. et al. Satellite-to-ground quantum key distribution. *Nature* **549**, 43–47 (2017).
46. Yin, J. et al. Satellite-based entanglement distribution over 1200 kilometers. *Science* **356**, 1140–1144 (2017).
47. Sun, Q.-C. et al. Entanglement swapping with independent sources over an optical-fiber network. *Phys. Rev. A* **95**, 032306 (2017).
48. Sun, Q.-C. et al. Entanglement swapping over 100 km optical fiber with independent entangled photon-pair sources. *Optica* **4**, 1214–1218 (2017).
49. Samara, F. et al. Entanglement swapping between independent and asynchronous integrated photon-pair sources. *Quantum Sci. Technol.* **6**, 045024 (2021).
50. Merkouche, S., Thiel, V., Davis, A. O. C. & Smith, B. J. Heralding multiple photonic pulsed bell pairs via frequency-resolved entanglement swapping. *Phys. Rev. Lett.* **128**, 063602 (2022).
51. Humble, T. S. & Grice, W. P. Effects of spectral entanglement in polarization-entanglement swapping and type-I fusion gates. *Phys. Rev. A* **77**, 022312 (2008).
52. Zopf, M. et al. Entanglement swapping with semiconductor-generated photons violates Bell's inequality. *Phys. Rev. Lett.* **123**, 160502 (2019).
53. Zhang, Y. et al. Simultaneous entanglement swapping of multiple orbital angular momentum states of light. *Nat. Commun.* **8**, 632 (2017).
54. Bouchard, F. et al. Two-photon interference: the Hong–Ou–mandel effect. *Rep. Prog. Phys.* **84**, 012402 (2020).
55. Baghdasaryan, B., Sevilla-Gutiérrez, C., Steinlechner, F. & Fritzsche, S. Generalized description of the spatio-temporal biphoton state in spontaneous parametric down-conversion. *Phys. Rev. A* **106**, 063711 (2022).
56. Sevilla-Gutiérrez, C. et al. Spectral properties of transverse Laguerre-Gauss modes in parametric down-conversion. *Phys. Rev. A* **109**, 023534 (2024).
57. Gouzien, E., Fedrici, B., Zavatta, A., Tanzilli, S. & D'Auria, V. Quantum description of timing jitter for single-photon on-off detectors. *Phys. Rev. A* **98**, 013833 (2018).
58. Takesue, H. & Shimizu, K. Effects of multiple pairs on visibility measurements of entangled photons generated by spontaneous parametric processes. *Opt. Commun.* **283**, 276–287 (2010).
59. Kuzucu, O., Fiorentino, M., Albota, M. A., Wong, F. N. C. & Kärtner, F. X. Two-photon coincident-frequency entanglement via extended phase matching. *Phys. Rev. Lett.* **94**, 083601 (2005).
60. Keller, U. Recent developments in compact ultrafast lasers. *Nature* **424**, 831–838 (2003).
61. Wakui, K. et al. Ultra-high-rate nonclassical light source with 50 ghz-repetition-rate mode-locked pump pulses and multiplexed single-photon detectors. *Opt. Express* **28**, 22399–22411 (2020).
62. Tsujimoto, Y., Wakui, K., Fujiwara, M., Sasaki, M. & Takeoka, M. Ultra-fast Hong-Ou-Mandel interferometry via temporal filtering. *Opt. Express* **29**, 37150–37160 (2021).
63. Cabrejo-Ponce, M., Spiess, C., Marques Muniz, A. L., Ancsin, P. & Steinlechner, F. Ghz-pulsed source of entangled photons for reconfigurable quantum networks. *Quantum Sci. Technol.* **7**, 045022 (2022).
64. Krzic, A., Heinig, D., Goy, M. & Steinlechner, F. Dual-downlink quantum key distribution with entangled photons: prospects for daylight operation. In *International Conference on Space Optics — ICSO 2022*, **12777**. https://doi.org/10.1117/12.2689971 (SPIE, 2023).
65. Bedington, R., Arrazola, J. M. & Ling, A. Progress in satellite quantum key distribution. *npj Quantum Inf.* **3**, 30 (2017).
66. Krämer, R. G. et al. Shaping the spectral response of ultrashort pulse phase mask written fiber Bragg gratings. *Opt. Express* **33**, 28152–28163 (2025).
67. Erdogan, T. Fiber grating spectra. *J. Lightwave Technol.* **15**, 1277–1294 (1997).

Acknowledgements

ML, SH, SN, and FS are part of the Max Planck School of Photonics supported by BMFTR, Max Planck Society, and Fraunhofer Society. This research was carried out within the scope of the QuNET project, funded by the German Federal Ministry of Research, Technology and Space (BMFTR) in the context of the federal government's research framework in IT security 'Digital. Secure. Sovereign. This work was co-funded by the Natural Sciences and Engineering Research Council of Canada (NSERC) and the European Commission under Grant no. 101070168 (HyperSpace) and the Carl-Zeiss-Stiftung within the Carl-Zeiss-Stiftung Center for Quantum Photonics (CZS QPhoton) under the project ID P2021-00-019. We also thank Carlos Sevilla-Gutiérrez for helpful discussions and Christopher Spiess for the code to perform post-selection of time tags.

Author contributions

B.B. wrote the main manuscript and developed the theoretical model. K.L.M. and M.C.P. performed the experiment. M.C.P. prepared Fig. 10, and M.L. prepared Fig. 9. B.B., K.J. and S.H. analyzed the accidental coincidences. B.B., K.L.M., M.C.P. and S.H. developed the data-processing code. B.B., M.L., C.A.M.L. and Y.T. investigated and calculated the photon rate–visibility trade-off and wrote the corresponding text. T.A.G., R.G.K. and S.N. manufactured the fiber Bragg gratings and helped analyze the filter response. T.G. measured the FBG power spectra. S.F. and Y.T. assisted with the storyline and strengthened the terminology. F.S. conceived the main idea and assisted in developing the theory and experiment. All authors reviewed the final manuscript.

Funding
Open Access funding enabled and organized by Projekt DEAL.

Competing interests
The authors declare no competing interests.

Additional information
Supplementary information The online version contains supplementary material available at https://doi.org/10.1038/s41534-026-01333-9.

Correspondence and requests for materials should be addressed to Baghdasar Baghdasaryan or Fabian Steinlechner.